

Dino U-Net: Exploiting High-Fidelity Dense Features from Foundation Models for Medical Image Segmentation

Yifan Gao^{1,2}, Haoyue Li¹, Feng Yuan¹, Xiaosong Wang^{2,3*}, and Xin Gao^{1*}

¹University of Science and Technology of China, Hefei, China

²Shanghai Innovation Institute, Shanghai, China

³Shanghai Artificial Intelligence Laboratory, Shanghai, China

*Corresponding author

Abstract—Foundation models pre-trained on large-scale natural image datasets offer a powerful paradigm for medical image segmentation. However, effectively transferring their learned representations for precise clinical applications remains a challenge. In this work, we propose Dino U-Net, a novel encoder-decoder architecture designed to exploit the high-fidelity dense features of the DINOv3 vision foundation model. Our architecture introduces an encoder built upon a frozen DINOv3 backbone, which employs a specialized adapter to fuse the model’s rich semantic features with low-level spatial details. To preserve the quality of these representations during dimensionality reduction, we design a new fidelity-aware projection module (FAPM) that effectively refines and projects the features for the decoder. We conducted extensive experiments on seven diverse public medical image segmentation datasets. Our results show that Dino U-Net achieves state-of-the-art performance, consistently outperforming previous methods across various imaging modalities. Our framework proves to be highly scalable, with segmentation accuracy consistently improving as the backbone model size increases up to the 7-billion-parameter variant. The findings demonstrate that leveraging the superior, dense-pretrained features from a general-purpose foundation model provides a highly effective and parameter-efficient approach to advance the accuracy of medical image segmentation. The code is available at <https://github.com/yifangao112/DinoUNet>.

Index Terms—DINOv3, Dino v3, foundation model, medical image segmentation

I. INTRODUCTION

Medical image segmentation is a foundational task in computer-aided diagnosis, providing quantitative analysis for clinical workflows such as disease screening, treatment planning, and longitudinal monitoring [1]–[7]. The accuracy and robustness of segmentation algorithms are therefore of utmost importance. The advent of deep learning, particularly the U-Net architecture [8], has revolutionized this field. With its effective encoder-decoder structure and skip connections, U-Net and its many variants have become the de-facto standard, demonstrating strong performance across a multitude of imaging modalities [9].

Recently, the emergence of foundation models, pre-trained on massive datasets, has initiated a paradigm shift in computer vision. Models like the Segment Anything Model (SAM) [10] have shown impressive zero-shot segmentation capabilities,

and subsequent works have explored adapting these models for medical applications [11]–[14]. However, the efficacy of these models is deeply connected to their pre-training objectives, which shape the nature of their learned features. SAM trained explicitly with segmentation masks, develop a strong inductive bias towards identifying boundaries of *natural world objects*.

In contrast, self-supervised foundation models learn a more general visual representation by capturing the intrinsic structure of images. This distinction is particularly relevant for medical segmentation. The DINO series of vision transformers has shown that features learned from unlabeled natural images can transfer remarkably well to specialized domains [15]–[17]. The latest iteration, DINOv3, represents a significant advancement by specifically addressing the challenge of dense feature degradation in large-scale training. Through its unique training objectives, DINOv3 produces dense representations of exceptional quality, surpassing prior models on tasks requiring precise spatial understanding. This presents a compelling opportunity to harness these high-fidelity features to overcome long-standing challenges in medical segmentation.

In this work, we introduce Dino U-Net, a novel hybrid architecture designed to exploit the superior dense features from DINOv3 for medical image segmentation. We propose an encoder built upon a frozen DINOv3 backbone, which uses a specialized adapter to fuse semantic and spatial information. We further design a fidelity-aware projection module to ensure that the rich details from the foundation model are effectively preserved and transferred to a U-Net decoder. Our central hypothesis is that by effectively harnessing the general-purpose, high-fidelity representations from DINOv3, we can significantly elevate the performance of a U-Net-based segmentation model across a wide spectrum of medical imaging tasks.

Our contributions are as follows:

- We propose Dino U-Net, a new architecture that successfully integrates a DINOv3-based encoder with a U-Net decoder.
- We design a new fidelity-aware projection module that preserves the quality of dense features during dimensionality reduction.

- We conduct extensive experiments on seven diverse public datasets, demonstrating that our method achieves state-of-the-art performance and generalizes well across different modalities.
- We show that our approach is highly parameter-efficient and scalable, with performance consistently improving as the foundation model size increases.

II. RELATED WORK

A. Medical image segmentation with foundation models

Foundation models, pre-trained on vast and diverse datasets, have introduced a new paradigm in computer vision by offering powerful, generalizable feature representations. In segmentation, the SAM and its successor, SAM2 [18], are prominent examples. These models leverage a prompt-based mechanism to achieve remarkable zero-shot segmentation capabilities. However, a notable domain gap between natural and medical images often necessitates further adaptation and fine-tuning to achieve optimal performance in clinical applications.

A particularly promising class of foundation models emerges from self-supervised learning, exemplified by the DINO series of vision transformers [15]. DINOv2 established that a transformer pre-trained on natural images could yield robust features that transfer remarkably well to medical segmentation [16]. The latest iteration, DINOv3 [17], represents a major leap forward. By scaling up the training data and model size and introducing techniques like Gram anchoring, DINOv3 produces exceptionally high-quality dense features. These features have been shown to surpass prior self-supervised models and even outperform specialized networks without task-specific fine-tuning. This development highlights a clear opportunity to harness these high-fidelity representations as a powerful encoder for complex downstream tasks like medical image segmentation.

B. Automatic medical image segmentation

While foundation models provide powerful encoders, the architectural design for precise segmentation remains critical. The U-Net continues to be the cornerstone architecture in medical imaging. Its encoder-decoder structure, complemented by skip connections, is exceptionally effective at capturing multi-scale contextual information while preserving the fine-grained spatial resolution necessary for accurate boundary delineation.

The success of U-Net has inspired numerous advancements. U-Net++ [19] and SegResNet [20] introduced dense and residual connections, respectively, to improve gradient flow and feature propagation. The nnU-Net framework automated the process of architectural configuration, establishing a robust baseline that consistently achieves state-of-the-art results [21]. More recent innovations such as U-Mamba [22] and U-KAN [23] have explored alternatives to standard convolutions by incorporating state space models and learnable activation functions to better capture long-range dependencies and enhance model expressiveness.

Critically, a trend towards hybrid models has emerged to combine the strengths of both research domains. For instance, SAM2 U-Net successfully integrated the backbone of SAM2 as an encoder within a U-Net decoder [24]. This confirmed the viability of using a foundation model’s feature extractor to power a proven segmentation architecture. However, the potential to leverage the superior dense features from the latest generation of self-supervised models like DINOv3 within such a hybrid framework has not been fully realized. Our work, Dino U-Net, is designed to fill this gap, investigating the hypothesis that the high-fidelity representations from DINOv3 can significantly elevate the performance of a U-Net-based segmentation model.

III. METHODOLOGY

A. Preliminary

Vision foundation models, pre-trained on vast datasets of diverse images, have demonstrated a remarkable ability to learn robust and generalizable visual representations. Among these, DINOv3 stands out as a particularly compelling choice for dense prediction tasks such as segmentation. DINOv3 is a self-supervised Vision Transformer, which learns its representations from large-scale, unlabeled natural image data without relying on explicit human annotations. This training paradigm encourages the model to capture a comprehensive understanding of visual scenes, including texture, shape, and context.

The primary advantage of DINOv3 lies in the exceptional quality of its dense features. Unlike its predecessors or other foundation models, DINOv3 was specifically engineered to address the degradation of patch-level feature maps during large-scale training. Through architectural enhancements and a novel training objective named Gram anchoring, it produces feature representations that are remarkably clean and coherent, showing superior performance in tasks that require precise spatial understanding. This proven ability to generate high-fidelity features from general-domain images presents a significant opportunity for medical image segmentation. These rich, dense-pretrained representations can provide a powerful inductive bias for segmenting complex anatomical structures, allowing our model to achieve a new level of accuracy and robustness.

B. Overview of the Dino U-Net

The overall architecture of our proposed Dino U-Net is illustrated in Figure 1. The proposed Dino U-Net follows an encoder-decoder structure, integrating a powerful feature extractor with a U-Net architecture highly effective for segmentation tasks. The overall design comprises an encoder path to capture hierarchical contextual information and a decoder path to perform precise localization for the final segmentation map.

The innovation of our work is centered on the encoder’s design, which is constructed upon a pre-trained and frozen DINOv3 foundation model. This encoder, denoted as E_{Dino} , generates a set of multi-scale skip connections S from an

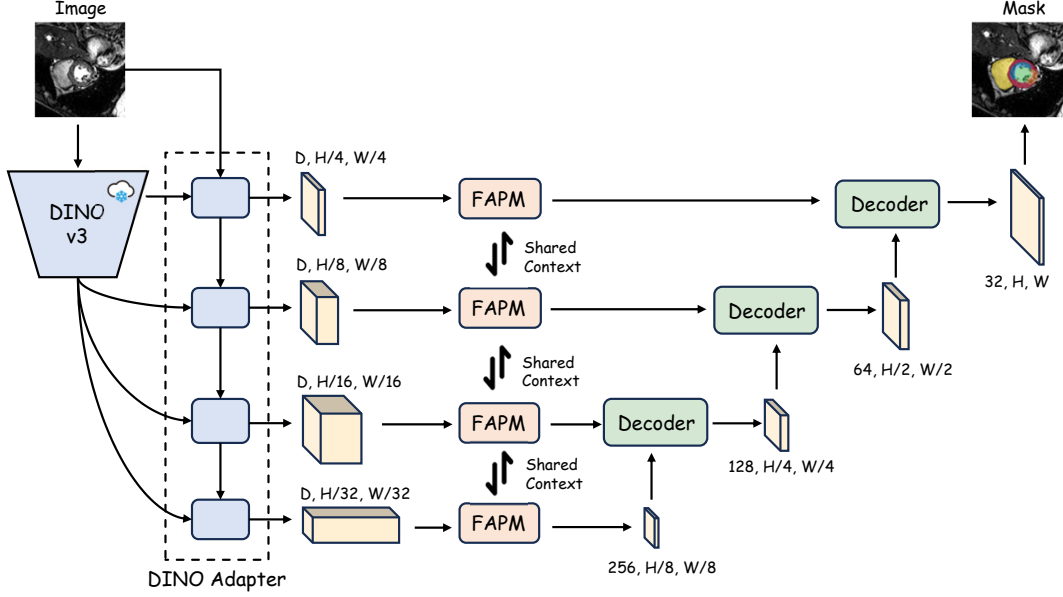


Fig. 1. An overview of our proposed Dino U-Net architecture. The model consists of an encoder built upon a frozen DINOv3 foundation model and a standard U-Net decoder. The encoder first employs an adapter. Subsequently, our proposed fidelity-aware projection module (FAPM) refines these enriched, multi-scale features and projects them to the channel dimensions required by the decoder. The resulting features are then passed as skip connections to the U-Net decoder to generate the final segmentation mask. Notably, only the adapter, FAPM, and decoder components are trainable.

input image X . These skip connections are then channeled to a standard U-Net decoder, D_{UNet} , which produces the final pixel-wise segmentation mask M . The entire operation can be expressed as:

$$M = D_{\text{UNet}}(S) = D_{\text{UNet}}(E_{\text{Dino}}(X)) \quad (1)$$

The encoder E_{Dino} operates through two sequential components. It first employs an adapter to produce a set of rich, multi-scale feature maps. Subsequently, our proposed fidelity-aware projection module (FAPM) processes these feature maps to refine their representations and project them into a suitable feature space for the decoder, yielding the final skip connections in S .

C. The DINOv3 Adapter

The adapter in the DINOv3 serves as the foundational component of our encoder, bridging the pre-trained backbone with the segmentation task. Its architecture is designed to effectively extract and combine features of different natures. It operates using a dual-branch design. One branch, the spatial prior module (SPM), processes the input image X to capture low-level spatial information and generate a set of multi-scale feature maps, $\{C_i\}_{i=1}^N$, where N is the number of scales.

$$\{C_i\}_{i=1}^N = \text{SPM}(X) \quad (2)$$

In parallel, the other branch leverages the frozen DINOv3 backbone, Φ_{DINOv3} , to extract powerful, high-level semantic features from several of its intermediate layers, resulting in a set of features $\{F_{\text{vit},i}\}_{i=1}^N$ corresponding to the same scales.

A simple fusion of these two feature sets would be suboptimal. Therefore, the adapter employs a series of interaction

blocks, IB_i , where the features from the convolutional branch are progressively enriched. The output of one stage, C'_{i-1} , becomes the input for the next interaction. Within each block, the spatial features act as queries to sample contextual information from the semantic features of the ViT backbone via a deformable cross-attention mechanism, \mathcal{A}_{de} . This iterative enrichment process can be formulated as:

$$C'_i = \text{IB}_i(C'_{i-1}, F_{\text{vit},i}) = \mathcal{A}_{\text{de}}(Q = C'_{i-1}, K = F_{\text{vit},i}, V = F_{\text{vit},i}) \quad (3)$$

where C'_0 is initialized from the initial SPM outputs. This process is repeated across multiple stages, ensuring a deep and effective fusion of spatial and semantic information. The final output of the adapter is a hierarchy of enriched feature maps $\{C'_i\}_{i=1}^N$ that are both spatially precise and semantically rich.

D. Fidelity-Aware Projection Module

The adapter produces a set of multi-scale feature maps that are exceptionally rich in semantic information. However, these features reside in a very high-dimensional space from the DINOv3 backbone, which is not directly compatible with the channel dimensions expected by a standard U-Net decoder. A naive projection, such as a simple linear layer or a 1×1 convolution, risks losing the fine-grained details and textural information that constitute the high-fidelity nature of these representations. To address this challenge and preserve the quality of the features during dimensionality reduction, we introduce the FAPM. The detailed structure of the FAPM is depicted in Figure 2.

The FAPM employs a design that disentangles shared contextual information from scale-specific details and uses the

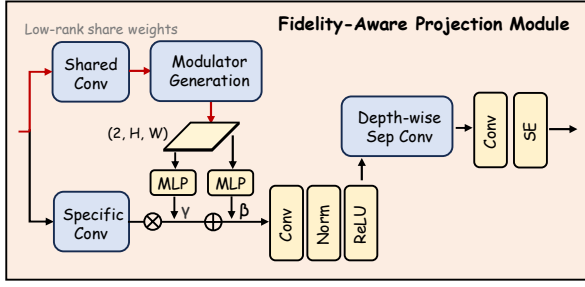


Fig. 2. The detailed architecture of our proposed FAPM. The module operates in two stages. First, in the orthogonal decomposition stage, multi-scale high-dimensional features are projected into a shared low-rank space using a 1x1 convolution. Second, in the progressive refinement stage, a dedicated block for each scale restores expressive capacity by using a depthwise separable convolution, a squeeze-and-excitation (SE) block, and a residual connection to produce the final high-fidelity features.

former to dynamically guide the latter. This process involves a dual-branch decomposition to extract these two types of information, followed by a feature-wise modulation step and a final refinement stage. Let the set of enriched, multi-scale feature maps from the adapter be $\{C'_i \in \mathbb{R}^{B \times D \times H_i \times W_i}\}_{i=1}^N$, where D is the high embedding dimension of the DINOv3 backbone and (H_i, W_i) are the spatial dimensions for each of the N scales.

First, the FAPM processes each feature map C'_i through two parallel branches that project the features into a common, intermediate-dimensional space of rank R . The shared context branch uses a single, shared 1x1 convolution with weights $W_{ctx} \in \mathbb{R}^{D \times R}$ to extract a scale-invariant contextual representation $Z_{ctx,i} \in \mathbb{R}^{B \times R \times H_i \times W_i}$. Concurrently, the specific feature branch uses a set of scale-dedicated 1x1 convolutions with weights $W_{sp,i} \in \mathbb{R}^{D \times R}$ to capture details unique to each scale, producing a feature map $Z_{sp,i} \in \mathbb{R}^{B \times R \times H_i \times W_i}$. These operations are defined as:

$$Z_{ctx,i} = W_{ctx}^T C'_i \quad \text{and} \quad Z_{sp,i} = W_{sp,i}^T C'_i \quad (4)$$

Instead of simple concatenation, we use the shared context to dynamically modulate the specific features. The contextual representation $Z_{ctx,i}$ is passed through a small, scale-specific generator network, \mathcal{G}_i , to produce a pair of modulation parameters: a scaling factor γ_i and a shifting factor β_i , both in $\mathbb{R}^{B \times R \times H_i \times W_i}$. These parameters perform a feature-wise linear modulation on $Z_{sp,i}$ to produce the modulated features $Z_{mod,i}$:

$$(\gamma_i, \beta_i) = \mathcal{G}_i(Z_{ctx,i}) \quad (5)$$

$$Z_{mod,i} = \gamma_i \odot Z_{sp,i} + \beta_i \quad (6)$$

where \odot denotes channel-wise multiplication. This modulation allows the shared context to recalibrate the scale-specific features in a spatially aware manner.

The modulated feature map, $Z_{mod,i}$, then enters a dedicated refinement block designed to enhance its expressive capacity while mapping it to the target channel dimension D'_i required by the U-Net decoder. The block first applies a scale-specific

1x1 convolution with weights $W_{r,i} \in \mathbb{R}^{R \times D'_i}$ to produce an initial feature map Y_i . This feature map then undergoes spatial refinement using a depthwise separable convolution, \mathcal{C}_{dwsep} , resulting in Y'_i .

$$Y_i = W_{r,i}^T Z_{mod,i} \quad \text{and} \quad Y'_i = \mathcal{C}_{dwsep}(Y_i) \quad (7)$$

To further improve feature discriminability, we employ a squeeze-and-excitation (SE) operation on Y'_i . A channel-wise attention vector $s_i \in \mathbb{R}^{D'_i}$ is generated by applying global average pooling (GAP) followed by a two-layer multi-layer perceptron (MLP) with a sigmoid activation σ .

$$s_i = \sigma(\text{MLP}(\text{GAP}(Y'_i))) \quad (8)$$

This attention vector recalibrates the spatially refined features. The complete operation of the refinement block, \mathcal{F}_{refine} , can be defined as the SE-recalibrated features. Finally, to ensure stable training and preserve information flow, we incorporate a residual connection that adds the block's input to its output. The final output of the FAPM for each scale, S_i , is computed as:

$$S_i = (Y'_i \odot s_i) + \mathcal{P}_i(Z_{mod,i}) \quad (9)$$

where \mathcal{P}_i is a projection shortcut (a 1x1 convolution or an identity mapping) that matches the channel dimensions of the input $Z_{mod,i}$ to the output. The resulting set of feature maps $\{S_i\}_{i=1}^N$ serves as the high-fidelity skip connections for the U-Net decoder.

E. Training Strategies

The parameters of the DINOv3 backbone are initialized using the weights pre-trained on LVD-1689M. The remaining trainable parameters, including those of the adapter, the FAPM, and the decoder, are initialized using a standard He initialization scheme. During the training process, only the parameters of the adapter, the FAPM, and the U-Net decoder are updated, while the DINOv3 backbone is kept frozen.

IV. EXPERIMENTS

A. Datasets

To comprehensively evaluate the effectiveness and generalization capabilities of our proposed Dino U-Net, we conducted extensive experiments on seven publicly available datasets. These datasets were selected to cover a wide spectrum of challenges in medical image segmentation, spanning diverse imaging modalities (e.g., MRI, Ultrasound, Endoscopy), various anatomical targets, and different pathologies. A detailed summary of the characteristics of each dataset is presented in Table I.

1) *Kvasir-SEG* [25]: This dataset is an endoscopic image collection aimed at the pixel-level segmentation of gastrointestinal polyps. Originally part of the MediaEval 2020 challenge, it contains 1000 polyp images, each with a corresponding ground truth segmentation mask annotated and verified by expert gastroenterologists.

TABLE I
SUMMARY OF THE SEVEN PUBLIC DATASETS USED FOR EVALUATION.

Dataset	Category	Modality	Target Classes	Cases
Kvasir-SEG [25]	Polyp	Endoscopy	Polyps	1000
Drishti-GS [26]	Optic Nerve Head	Fundus	Optic Disc & Cup	101
BUSI [27]	Breast Tumor	Ultrasound	Benign & Malignant Tumors	780
CellBinDB [28]	Cell	Microscopy	Cells (Mouse & Human)	1044
MyoPS20 [29]–[31]	Myocardial Pathology	CMR	Scar, Edema, Myocardium, LV/RV Pools	25
PROSTATEx-Seg-Zones [32]	Gland	MRI	4 Prostate Zones	98
m2caiSeg [33]	Surgical Instrument	Endoscopy	19 classes (Organs, Instruments, Fluids)	307

2) *Drishti-GS* [26]: This dataset provides color fundus images for the segmentation of the optic nerve head, specifically the optic disc and cup, to aid in automated glaucoma assessment. It contains 101 retinal images.

3) *BUSI* [27]: This dataset is designed for the segmentation and classification of breast tumors in 2D ultrasound images. It consists of 780 images from 600 female patients, categorized into normal, benign, and malignant classes. For benign and malignant images, corresponding ground truth masks of the tumors are provided.

4) *CellBinDB* [28]: This dataset is designed for the development of cell segmentation models, containing a total of 1044 microscopy images. The collection includes 844 images from 30 mouse tissues and 200 images from 5 human tissues, originally gathered from 10x Genomics. For all images, both instance-level and semantic segmentation masks are provided.

TABLE II
EXPERIMENTAL CONFIGURATIONS FOR PATCH SIZE AND BATCH SIZE FOR EACH DATASET, AS DETERMINED BY THE nnU-NET PLANNING PROCESS.

Dataset	Patch Size	Batch Size
Kvasir-SEG	(448, 448)	18
Drishti-GS	(256, 256)	5
BUSI	(448, 448)	18
CellBinDB	(512, 512)	13
MyoPS20	(512, 512)	6
PROSTATEx-Seg-Zones	(512, 512)	13
m2caiSeg	(768, 768)	6

5) *MyoPS20* [29]–[31]: This dataset focuses on myocardial pathology segmentation by combining multi-sequence cardiac magnetic resonance (CMR) imaging. It contains aligned T2, bSSFP, and LGE CMR scans from 25 patients, with manual annotations for scar, edema, normal myocardium, and the left and right ventricular blood pools.

6) *PROSTATEx-Seg-Zones* [32]: This dataset provides zonal segmentations for prostate glands using transversal T2-weighted MRI scans. It contains 98 cases randomly selected from the SPIE-AAPM-NCI PROSTATEx Challenge. The expert-verified, four-class annotations encompass the peripheral zone, transition zone, fibromuscular stroma, and the distal prostatic urethra.

7) *m2caiSeg* [33]: This dataset provides endoscopic images for the segmentation of various structures and instruments during surgical procedures. It was created by sampling and

pixel-level annotating 307 frames from two videos of the MICCAI 2016 Surgical Tool Detection dataset.

B. Comparison methods and metrics

We compare it against a suite of seven state-of-the-art medical image segmentation models. These baselines include established convolutional architectures such as nnU-Net, SegResNet, and UNet++. We also include more recent methods that incorporate novel designs, such as U-Mamba and U-KAN, which explore different architectural principles. Furthermore, to provide a comprehensive comparison against other foundation model-based approaches, we include Swin U-Mamba† [34] and SAM2-UNet [24] in our evaluation.

We evaluate segmentation accuracy using the Dice Similarity Coefficient (Dice) to measure volumetric overlap (higher is better) and the 95% Hausdorff Distance (HD95) to assess boundary correspondence (lower is better). In addition to segmentation accuracy, we assess model efficiency by reporting the number of activated parameters. This metric reflects the number of trainable weights in each model, with a lower count indicating a more parameter-efficient architecture.

C. Implementation details

To ensure a fair and reproducible comparison, all experiments were conducted within the PyTorch framework and followed the standardized pipeline of the nnU-Net framework. For each dataset, we performed a random 80-20 split to create training and testing sets. The raw data was preprocessed according to the nnU-Net scheme, where images are resampled to a fixed patch size based on the median size of the dataset’s foreground classes. The batch size for each experiment was also determined by the plan file generated by nnU-Net (Table II). The network is trained in a supervised manner using a combined loss function, which is a summation of the Dice loss and the cross-entropy loss. We set the rank of the low-dimensional space R to 256. We train our model using the Adam optimizer with an initial learning rate of 1×10^{-3} and a batch size determined by our data configuration for 200 epochs. During training, we applied the comprehensive online data augmentation suite from nnU-Net to all methods, including elastic deformations, random rotations, and scaling. All models were trained for 200 epochs, with each epoch consisting of 250 mini-batches, using the Adam optimizer and a polynomial learning rate decay schedule. For evaluation, the model checkpoint from the final training epoch was used to

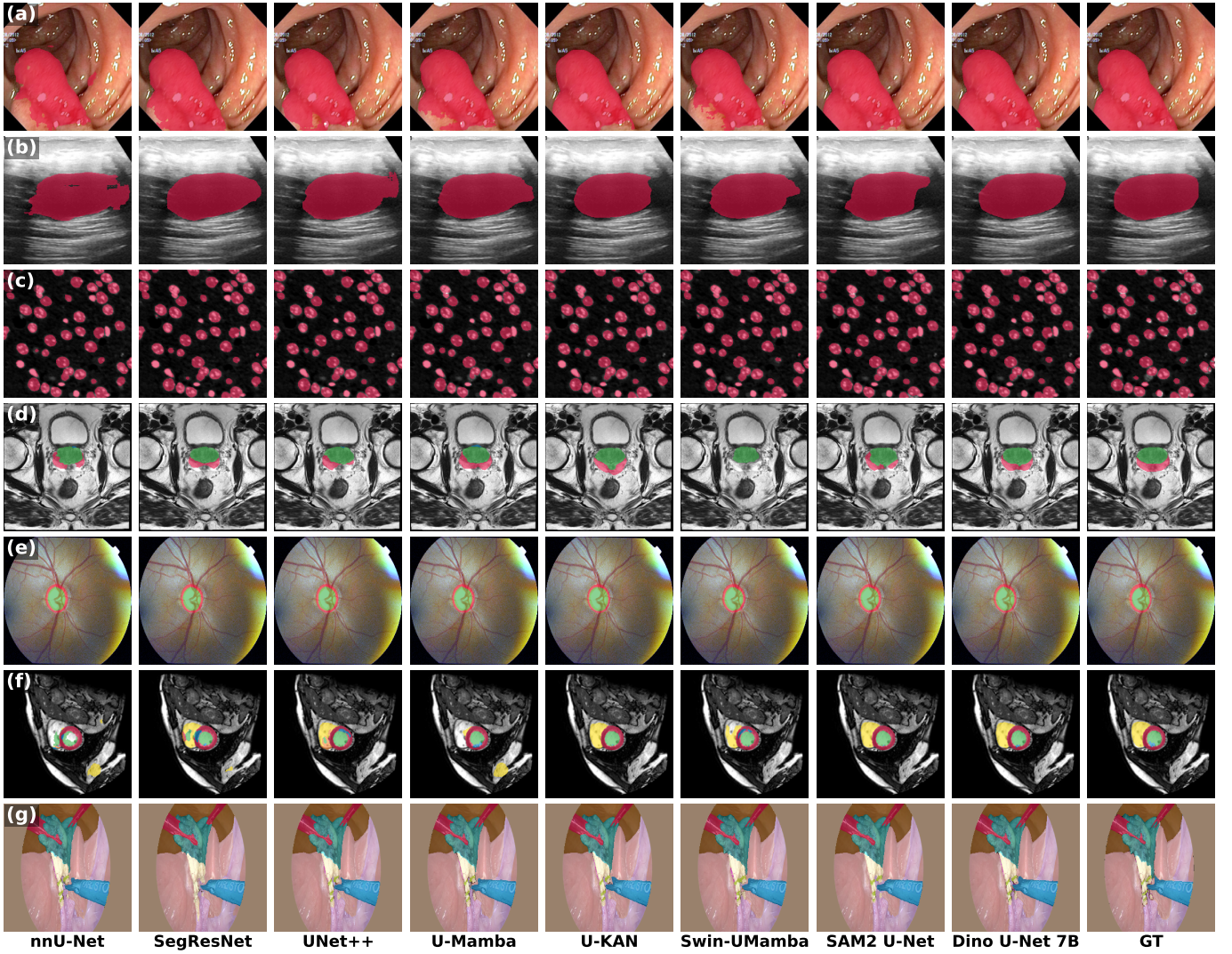


Fig. 3. Qualitative comparison of segmentation results on representative samples from the seven evaluated datasets. Each column displays a different method, while each row corresponds to a different dataset (from top to bottom: Kvasir-SEG, Drishti-GS, BUSI, CellBinDB, MyoPS20, PROSTATEx-Seg-Zones, and m2caiSeg). Our proposed Dino U-Net demonstrate superior boundary delineation and produce more complete segmentation masks compared to the baseline methods.

perform inference on the test set. The inference was conducted using a sliding window approach with Gaussian importance weighting to ensure smooth predictions at patch boundaries. All experiments were performed on NVIDIA H100 GPUs.

D. Results

The quantitative results of our extensive evaluation are presented in Table III and Table IV. Figure 3 provides a qualitative comparison, visually demonstrating the superior performance of our method on representative examples. Our proposed Dino U-Net architecture demonstrates a consistent and significant performance improvement over all seven state-of-the-art baseline methods across the diverse range of medical imaging datasets.

As detailed in Table III, our Dino U-Net variants achieve superior performance on both the Dice Similarity Coefficient and the 95% Hausdorff Distance metrics in the majority of

cases. Notably, the Dino U-Net 7B model establishes a new state of the art on five of the seven datasets in terms of Dice score, showing its robustness across different imaging modalities, from endoscopy (Kvasir-SEG, m2caiSeg) and microscopy (CellBinDB) to MRI (MyoPS20, PROSTATEx). A clear trend of performance improvement is also observable as the DINOv3 backbone scales from the Small (S) to the 7B version, indicating that our architecture effectively leverages the enhanced representational power of larger foundation models. Even our most compact model, Dino U-Net S, outperforms the strongest baselines on several datasets, such as achieving the best Dice and HD95 scores on the Drishti-GS dataset.

Table IV provides an overall summary of model performance and efficiency. Our largest model, Dino U-Net 7B, achieves the best average Dice score of 76.43% and the best average HD95 of 18.76, representing a substantial improve-

TABLE III

COMPARISON OF SEGMENTATION PERFORMANCE ON SEVEN MEDICAL DATASETS. WE REPORT THE DICE SIMILARITY COEFFICIENT (%) AND THE HD95. FOR THE DICE SCORE, HIGHER IS BETTER (\uparrow); FOR HD95, LOWER IS BETTER (\downarrow). FOR OUR DINOUNET VARIANTS, SCORES OUTPERFORMING THE BEST BASELINE ARE MARKED IN **BOLD**, AND SCORES OUTPERFORMING THE SECOND-BEST BASELINE ARE UNDERLINED.

Method	Kvasir-SEG		Drishiti-GS		BUSI		CellBinDB		MyoPS20		PROSTATEx		m2caiseg	
	Dice \uparrow	HD95 \downarrow	Dice \uparrow	HD95 \downarrow	Dice \uparrow	HD95 \downarrow	Dice \uparrow	HD95 \downarrow	Dice \uparrow	HD95 \downarrow	Dice \uparrow	HD95 \downarrow	Dice \uparrow	HD95 \downarrow
nnU-Net [21]	80.85	61.48	82.94	1.60	65.51	77.06	87.82	2.71	61.98	22.46	69.52	5.11	51.55	50.48
SegResNet [20]	85.98	35.08	82.91	1.62	67.83	64.95	87.03	3.12	67.60	14.24	71.93	4.62	43.18	53.72
UNet++ [19]	85.69	44.08	82.82	1.65	68.96	66.63	87.43	2.89	67.42	16.33	71.82	4.76	49.80	43.03
U-Mamba [22]	85.24	40.91	82.16	1.78	68.53	56.05	87.74	3.15	62.51	28.00	72.02	4.89	52.49	45.74
U-KAN [23]	85.33	41.32	83.89	1.48	68.29	44.88	86.99	3.92	73.59	11.15	72.65	4.54	51.01	45.28
Swin U-Mamba \dagger [34]	81.16	59.59	80.06	2.03	66.43	66.20	86.90	3.15	70.39	11.00	69.81	5.57	44.65	51.94
SAM2-U-Net [24]	89.79	27.07	83.43	1.64	66.04	59.20	87.23	3.22	74.07	10.39	71.67	4.39	49.70	52.74
Dino U-Net S	88.87	33.24	84.19	1.43	71.87	58.40	87.38	2.80	74.92	10.21	72.02	4.16	51.13	52.08
Dino U-Net B	<u>88.56</u>	<u>28.03</u>	83.90	1.47	70.78	57.36	87.56	3.19	75.41	8.39	<u>72.19</u>	4.38	52.39	47.23
Dino U-Net L	<u>89.63</u>	<u>27.81</u>	84.41	1.40	71.25	56.44	<u>87.51</u>	2.53	74.22	<u>10.49</u>	<u>72.50</u>	4.33	52.78	45.53
Dino U-Net 7B	90.77	25.44	84.48	1.48	70.63	<u>46.85</u>	87.92	2.64	74.63	8.35	73.09	<u>4.53</u>	53.46	42.01

TABLE IV

OVERALL COMPARISON OF MODEL EFFICIENCY AND AVERAGE PERFORMANCE. EFFICIENCY IS MEASURED BY THE NUMBER OF ACTIVATED PARAMETERS (PARAMS). WE REPORT THE AVERAGE DICE (%) AND HD95. THE BEST RESULT IN EACH COLUMN IS IN **BOLD**. FOR DINOUNET VARIANTS, THE IMPROVEMENT OVER THE BEST-PERFORMING BASELINE MODEL IS SHOWN IN **RED**.

Method	Params (M) \downarrow	Avg. Dice (%) \uparrow	Avg. HD95 \downarrow
nnU-Net [21]	30.451	71.45	31.56
SegResNet [20]	10.263	72.35	25.34
UNet++ [19]	14.387	73.42	25.62
U-Mamba [22]	63.763	72.96	25.79
U-KAN [23]	9.382	74.54	21.80
Swin U-Mamba \dagger [34]	37.763	71.34	28.50
SAM2-U-Net [24]	5.380	74.56	22.66
Dino U-Net S	5.106	75.77 (+1.21)	23.19
Dino U-Net B	11.651	75.83 (+1.27)	21.44 (-0.36)
Dino U-Net L	18.144	76.04 (+1.48)	21.22 (-0.58)
Dino U-Net 7B	228.968	76.43 (+1.87)	18.76 (-3.04)

ment of 1.87 points in Dice and 3.04 points in HD95 over the best-performing baseline model. Furthermore, our approach demonstrates exceptional parameter efficiency. The Dino U-Net S model, with only 5.106 million activated parameters, is the most lightweight model in our comparison yet surpasses the performance of all baseline methods on average. This highlights our method’s ability to achieve superior segmentation accuracy while maintaining a highly efficient architecture.

E. Ablation Study

To validate the effectiveness of our proposed FAPM, we conducted an ablation study by removing it from our Dino U-Net architecture. For this experiment, the FAPM was replaced with a baseline projection block consisting of simple 1x1 convolutions for each scale. The results of this study are presented in Figure 4. Our analysis focuses on two aspects: parameter efficiency and segmentation performance.

The first part of our study, shown in Figure 4(a), examines the impact of FAPM on the model’s parameter count. An interesting trend emerges: for our largest 7B model, replacing FAPM with simple convolutions leads to a parameter increase

from 228.97M to 229.81M. Conversely, for the smaller S, B, and L models, this replacement results in a slight parameter reduction. This observation highlights the efficiency of FAPM’s low-rank, shared-basis design, which becomes more parameter-efficient than separate projection layers as the backbone’s feature dimension grows.

The second part of our study, illustrated in Figure 4(b), analyzes the performance degradation when FAPM is removed. We observe a consistent decline in segmentation accuracy across all model scales. The Dice scores decrease by a margin of 0.56% to 0.79%, while the HD95 metric worsens by 0.09mm to 1.75mm. This degradation underscores the importance of the sophisticated feature projection and refinement process provided by FAPM. The notable increase in the HD95 metric, in particular, indicates that the high-fidelity features preserved by FAPM are especially beneficial for improving the precision of boundary delineation. Collectively, these results confirm that our proposed FAPM is a crucial component that enhances both the accuracy and, for larger models, the parameter efficiency of the Dino U-Net architecture.

V. DISCUSSION

In this work, we proposed Dino U-Net, an architecture that successfully integrates a large-scale, pre-trained vision foundation model into a U-Net for medical image segmentation. Our experimental results consistently demonstrate that this approach achieves state-of-the-art performance across a wide array of medical imaging tasks. This section discusses the key insights derived from our findings and the broader implications of our approach.

A central insight from our work is that a general-purpose visual understanding, as learned by DINOv3, can be more effective for medical segmentation than the features from a model specifically optimized for segmentation, such as SAM. The encoder in SAM is trained with segmentation masks, biasing its feature space towards identifying object boundaries and contours. In contrast, DINOv3 learns the underlying structure of the visual world through self-supervision without any explicit segmentation guidance. This allows it to capture a richer set of visual properties, including texture, material, and

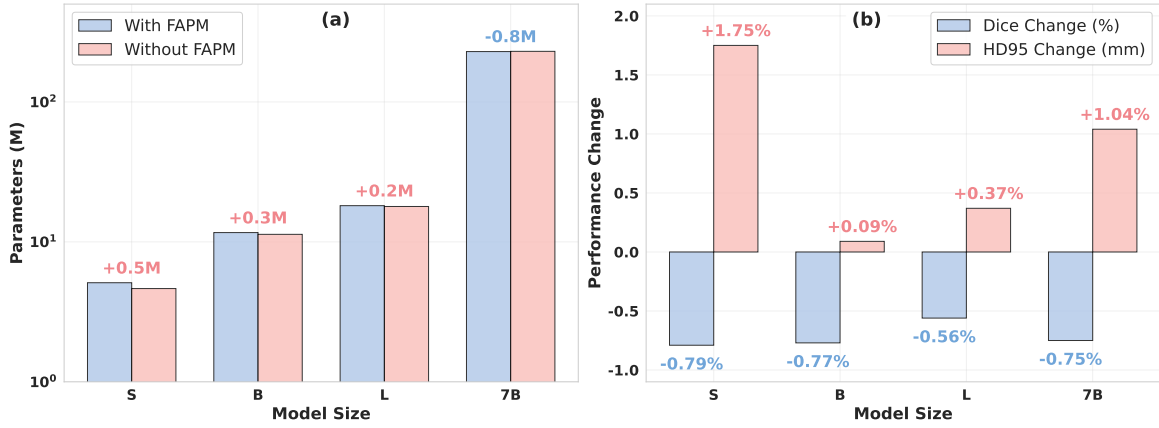


Fig. 4. Ablation study on the proposed FAPM. (a) Parameter comparison between models with and without FAPM across different scales (S, B, L, 7B). Replacing FAPM with baseline convolutions leads to a parameter increase for the 7B model (from 228.97M to 229.81M), while smaller models exhibit slight parameter reductions. This observation highlights FAPM’s parameter-sharing mechanism. (b) Performance degradation analysis when FAPM is removed, showing the importance of sophisticated feature projection for segmentation accuracy. Dice scores decrease by 0.56-0.79%, while HD95 metrics worsen by 0.09-1.75mm, indicating that FAPM improves boundary precision.

context, which are often essential for differentiating between ambiguous tissue types in medical images. Our results suggest that this deeper semantic understanding provides a more robust foundation for segmentation, especially when dealing with low-contrast regions or novel pathologies, outperforming an encoder that is primarily focused on finding edges.

Furthermore, the performance gains observed as we scale the Dino U-Net from the small (S) to the 7B variant reveal the significant potential of this approach. The consistent improvement with larger backbones indicates that medical image segmentation has not yet reached a performance plateau and can continue to benefit from the enhanced representational power of even larger foundation models. This scaling trend suggests that the rich, hierarchical features learned by billion-parameter models contain a depth of information that smaller, domain-specific models cannot capture. Our architecture proves to be an effective vehicle for transferring this power to the medical domain.

The success of our architecture also hinges on the fidelity-aware projection module. The ablation study confirms its importance, as its removal leads to a notable drop in performance. The challenge in using a large foundation model like DINOv3 is to translate its very high-dimensional features for a decoder without losing the fine-grained details that make them so powerful. The FAPM addresses this by first identifying the core feature components through a low-rank projection and then selectively refining them. This projection mechanism is key to preserving the high-fidelity information from the encoder, which is particularly evident in the improved HD95 metric, confirming its role in achieving precise boundary delineation.

Our work also highlights the remarkable parameter efficiency of using a frozen foundation model encoder. By only training the adapter, FAPM, and decoder, our method achieves state-of-the-art results while being computationally efficient during the training phase. This makes our approach

particularly attractive for the medical imaging domain, where datasets are often not large enough to support the training of very deep networks from scratch without the risk of overfitting.

While our results are promising, we also recognize some limitations. The current Dino U-Net architecture is designed for 2D image segmentation and its extension to 3D volumetric data, such as CT or MRI scans, remains an important area for future work. Additionally, while the number of trainable parameters is small, the inference process for the largest 7B model still requires significant computational resources due to the size of the frozen backbone. Future research could explore techniques like knowledge distillation to create more compact yet powerful models.

VI. CONCLUSION

In this paper, we presented Dino U-Net, a new architecture that successfully integrates the DINOv3 foundation model as a powerful encoder for medical image segmentation. Our method employs a specialized adapter and a novel fidelity-aware projection module to effectively harness the high-fidelity dense features learned from large-scale, general-domain data. Through comprehensive experiments on seven public datasets, we demonstrated that our approach significantly outperforms existing state-of-the-art models, showcasing its strong performance and generalization capabilities across different medical imaging modalities. Our work confirms the hypothesis that the rich, dense-pretrained representations from the latest generation of self-supervised foundation models can provide a more effective inductive bias for medical segmentation than training specialized models from scratch. Future work will focus on extending this 2D framework to 3D volumetric segmentation tasks.

REFERENCES

- [1] X. Mei, H.-C. Lee, K.-y. Diao, M. Huang, B. Lin, C. Liu, Z. Xie, Y. Ma, P. M. Robson, M. Chung *et al.*, “Artificial intelligence-enabled rapid

- diagnosis of patients with covid-19,” *Nature medicine*, vol. 26, no. 8, pp. 1224–1228, 2020.
- [2] A. Shaker, M. Maaz, H. Rasheed, S. Khan, M.-H. Yang, and F. S. Khan, “Unetr++: delving into efficient and accurate 3d medical image segmentation,” *IEEE Transactions on Medical Imaging*, vol. 43, no. 9, pp. 3377–3390, 2024.
 - [3] H.-Y. Zhou, J. Guo, Y. Zhang, X. Han, L. Yu, L. Wang, and Y. Yu, “nn-former: Volumetric medical image segmentation via a 3d transformer,” *IEEE transactions on image processing*, vol. 32, pp. 4036–4045, 2023.
 - [4] Y. Dai, Y. Gao, and F. Liu, “Transmed: Transformers advance multi-modal medical image classification,” *Diagnostics*, vol. 11, no. 8, p. 1384, 2021.
 - [5] Y. Gao, Y. Dong, W. Wu, C. Ge, F. Yuan, J. Sheng, H. Li, and X. Gao, “Wega: Weakly-supervised global-local affinity learning framework for lymph node metastasis prediction in rectal cancer,” *arXiv preprint arXiv:2505.10502*, 2025.
 - [6] Y. Gao, Y. Dai, F. Liu, W. Chen, and L. Shi, “An anatomy-aware framework for automatic segmentation of parotid tumor from multimodal mri,” *Computers in Biology and Medicine*, vol. 161, p. 107000, 2023.
 - [7] Y. Gao, S. Rui, H. Su, J. Xiang, L. Wu, and X. Wang, “A composite alignment-aware framework for myocardial lesion segmentation in multi-sequence cmr images,” *arXiv preprint arXiv:2507.11886*, 2025.
 - [8] O. Ronneberger, P. Fischer, and T. Brox, “U-net: Convolutional networks for biomedical image segmentation,” in *International Conference on Medical image computing and computer-assisted intervention*. Springer, 2015, pp. 234–241.
 - [9] M. Krithika Alias AnbuDevi and K. Suganthi, “Review of semantic segmentation of medical images using modified architectures of unet,” *Diagnostics*, vol. 12, no. 12, p. 3064, 2022.
 - [10] A. Kirillov, E. Mintun, N. Ravi, H. Mao, C. Rolland, L. Gustafson, T. Xiao, S. Whitehead, A. C. Berg, W.-Y. Lo *et al.*, “Segment anything,” in *Proceedings of the IEEE/CVF international conference on computer vision*, 2023, pp. 4015–4026.
 - [11] C. Chen, J. Miao, D. Wu, A. Zhong, Z. Yan, S. Kim, J. Hu, Z. Liu, L. Sun, X. Li *et al.*, “Ma-sam: Modality-agnostic sam adaptation for 3d medical image segmentation,” *Medical Image Analysis*, vol. 98, p. 103310, 2024.
 - [12] Y. Zhang, Z. Shen, and R. Jiao, “Segment anything model for medical image segmentation: Current applications and future directions,” *Computers in Biology and Medicine*, vol. 171, p. 108238, 2024.
 - [13] J. Wu, Z. Wang, M. Hong, W. Ji, H. Fu, Y. Xu, M. Xu, and Y. Jin, “Medical sam adapter: Adapting segment anything model for medical image segmentation,” *Medical image analysis*, vol. 102, p. 103547, 2025.
 - [14] Y. Gao, J. Sheng, W. Wu, H. Li, Y. Dong, C. Ge, F. Yuan, and X. Gao, “Safeclck: Error-tolerant interactive segmentation of any medical volumes via hierarchical expert consensus,” *arXiv preprint arXiv:2506.18404*, 2025.
 - [15] H. Zhang, F. Li, S. Liu, L. Zhang, H. Su, J. Zhu, L. M. Ni, and H.-Y. Shum, “Dino: Detr with improved denoising anchor boxes for end-to-end object detection,” *arXiv preprint arXiv:2203.03605*, 2022.
 - [16] M. Oquab, T. Darcet, T. Moutakanni, H. Vo, M. Szafraniec, V. Khalidov, P. Fernandez, D. Haziza, F. Massa, A. El-Nouby *et al.*, “Dinov2: Learning robust visual features without supervision,” *arXiv preprint arXiv:2304.07193*, 2023.
 - [17] O. Siméoni, H. V. Vo, M. Seitzer, F. Baldassarre, M. Oquab, C. Jose, V. Khalidov, M. Szafraniec, S. Yi, M. Ramamonjisoa, F. Massa, D. Haziza, L. Wehrstedt, J. Wang, T. Darcet, T. Moutakanni, L. Sentana, C. Roberts, A. Vedaldi, J. Tolan, J. Brandt, C. Couprie, J. Mairal, H. Jégou, P. Labatut, and P. Bojanowski, “DINOv3,” 2025. [Online]. Available: <https://arxiv.org/abs/2508.10104>
 - [18] N. Ravi, V. Gabeur, Y.-T. Hu, R. Hu, C. Ryali, T. Ma, H. Khedr, R. Rädle, C. Rolland, L. Gustafson *et al.*, “Sam 2: Segment anything in images and videos,” *arXiv preprint arXiv:2408.00714*, 2024.
 - [19] Z. Zhou, M. M. R. Siddiquee, N. Tajbakhsh, and J. Liang, “Unetr++: Redesigning skip connections to exploit multiscale features in image segmentation,” *IEEE transactions on medical imaging*, vol. 39, no. 6, pp. 1856–1867, 2019.
 - [20] A. Myronenko, “3d mri brain tumor segmentation using autoencoder regularization,” in *International MICCAI brainlesion workshop*. Springer, 2018, pp. 311–320.
 - [21] F. Isensee, P. F. Jaeger, S. A. Kohl, J. Petersen, and K. H. Maier-Hein, “nnu-net: a self-configuring method for deep learning-based biomedical image segmentation,” *Nature methods*, vol. 18, no. 2, pp. 203–211, 2021.
 - [22] J. Ma, F. Li, and B. Wang, “U-mamba: Enhancing long-range dependency for biomedical image segmentation,” *arXiv preprint arXiv:2401.04722*, 2024.
 - [23] C. Li, X. Liu, W. Li, C. Wang, H. Liu, Y. Liu, Z. Chen, and Y. Yuan, “U-kan makes strong backbone for medical image segmentation and generation,” in *Proceedings of the AAAI Conference on Artificial Intelligence*, vol. 39, no. 5, 2025, pp. 4652–4660.
 - [24] X. Xiong, Z. Wu, S. Tan, W. Li, F. Tang, Y. Chen, S. Li, J. Ma, and G. Li, “Sam2-unet: Segment anything 2 makes strong encoder for natural and medical image segmentation,” *arXiv preprint arXiv:2408.08870*, 2024.
 - [25] D. Jha, P. H. Smedsrud, M. A. Riegler, P. Halvorsen, T. de Lange, D. Johansen, and H. D. Johansen, “Kvasir-seg: A segmented polyp dataset,” in *MultiMedia Modeling: 26th International Conference, MMM 2020, Daejeon, South Korea, January 5–8, 2020, Proceedings, Part II* 26. Springer, 2020, pp. 451–462.
 - [26] J. Sivaswamy, S. R. Krishnadas, G. Datt Joshi, M. Jain, and A. U. Syed Tabish, “Drishti-gs: Retinal image dataset for optic nerve head(onh) segmentation,” in *2014 IEEE 11th International Symposium on Biomedical Imaging (ISBI)*, 2014, pp. 53–56.
 - [27] W. Al-Dhabyani, M. Gomaa, H. Khaled, and A. Fahmy, “Dataset of breast ultrasound images,” *Data in brief*, vol. 28, p. 104863, 2020.
 - [28] C. Shi, J. Fan, Z. Deng, H. Liu, Q. Kang, Y. Li, J. Guo, J. Wang, J. Gong, S. Liao *et al.*, “Cellbindb: a large-scale multimodal annotated dataset for cell segmentation with benchmarking of universal models,” *GigaScience*, vol. 14, p. g1af069, 2025.
 - [29] S. Gao, H. Zhou, Y. Gao, and X. Zhuang, “Bayeseg: Bayesian modeling for medical image segmentation with interpretable generalizability,” *Medical image analysis*, vol. 89, p. 102889, 2023.
 - [30] X. Zhuang, “Multivariate mixture model for myocardial segmentation combining multi-source images,” *IEEE transactions on pattern analysis and machine intelligence*, vol. 41, no. 12, pp. 2933–2946, 2018.
 - [31] J. Qiu, L. Li, S. Wang, K. Zhang, Y. Chen, S. Yang, and X. Zhuang, “Myops-net: Myocardial pathology segmentation with flexible combination of multi-sequence cmr images,” *Medical image analysis*, vol. 84, p. 102694, 2023.
 - [32] A. Meyer, D. Schindele, D. Von Reibnitz, M. Rak, M. Schostak, and C. Hansen, “Prostatex zone segmentations [data set],” *The Cancer Imaging Archive*, p. 131, 2020.
 - [33] S. Maqbool, A. Riaz, H. Sajid, and O. Hasan, “m2caiseg: Semantic segmentation of laparoscopic images using convolutional neural networks,” *arXiv preprint arXiv:2008.10134*, 2020.
 - [34] J. Liu, H. Yang, H.-Y. Zhou, Y. Xi, L. Yu, C. Li, Y. Liang, G. Shi, Y. Yu, S. Zhang *et al.*, “Swin-umamba: Mamba-based unet with imagenet-based pretraining,” in *International conference on medical image computing and computer-assisted intervention*. Springer, 2024, pp. 615–625.